POLITECNICO DI TORINO
Repository ISTITUZIONALE

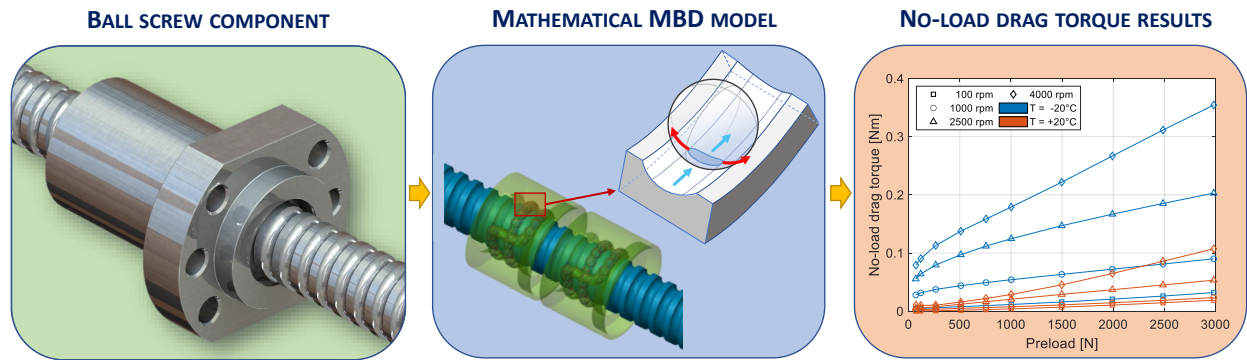Investigation on the ball screws no-load drag torque in presence of lubrication through MBD simulations

(Article begins on next page)

01 September 2025

Graphical Abstract

Investigation on the Ball Screws No-Load Drag Torque in Presence of Lubrication through MBD Simulations

Antonio Carlo Bertolino, Giovanni Jacazio, Stefano Mauro, Massimo Sorli

BALL SCREW COMPONENT

MATHEMATICAL MBD MODEL

NO-LOAD DRAG TORQUE RESULTS

Highlights

Investigation on the Ball Screws No-Load Drag Torque in Presence of Lubrication through MBD Simulations

Antonio Carlo Bertolino, Giovanni Jacazio, Stefano Mauro, Massimo Sorli

- A fully comprehensive multibody dynamic model of ball screws is presented

- A simplified lubricated friction model is used to describe sphere-groove interactions

- The no-load drag torque highly depends on temperature due to lubricant viscosity

- The choice of the correct lubricant is paramount to reduce friction and wear

Investigation on the Ball Screws No-Load Drag Torque in Presence of Lubrication through MBD Simulations

Antonio Carlo Bertolino*, Giovanni Jacazio, Stefano Mauro, Massimo Sorli

Department of Mechanical and Aerospace Engineering
Politecnico di Torino, Corso Duca degli Abruzzi 24, 10129, Turin, Italy

Abstract

The no-load drag torque is a crucial factor in the design phase to estimate the power required by the electric motor in electro-mechanical actuators (EMA). This paper focuses on the analysis of the drag torque contribution generated in preloaded double nut ball screws of EMAs. In literature its value is commonly estimated with a linear relationship with respect to the preload level. However, many other parameters play a role in determining the friction torque, such as operating speed, temperature and geometry. A sensitivity analysis on these parameters is presented by means of simulation results obtained from a high-fidelity multi-body dynamic (MBD) model, capable of describing the full three-dimensional dynamics of each subcomponent and the presence of full film, mixed or boundary lubrication between mating elements. The results have been interpreted with a physics-based approach highlighting a strong dependency of the drag torque on temperature basing on the lubricant's viscosity. This parameter also influences the drag torque speed dependence, which resulted to be more pronounced for low operating temperatures. An experimental test bench is being constructed to validate the model results.

Keywords: Electro-mechanical actuator, Ball screw, MBD simulations, No-load drag torque, Lubrication

1. Introduction

Born from environmental and cost saving concerns, the recent trend toward "more electric" aircraft has touched most of the more important on-board systems and equipment [1, 2, 3]. For flight control devices, this tendency translated into several and still concurring efforts to replace the traditional electro-hydraulic configuration (EHSAs) with electro-mechanical actuators (EMAs) for primary and secondary aerodynamic surfaces [4, 5, 6, 7], a technology already widely spread in several fields, such as the manufacturing industry [8].

EMAs theoretically provide several advantages over the hydraulic solution in terms of envelope, weight, environment pollution and so forth. The expected life and performance of

---

EMAs is strictly dependent on design and control parameters [9, 10]. Their widespread use is however hindered by a higher jamming probability, which is beyond the imposed/required limit for flight safety critical applications [11]. To overcome this issue, several solutions have been proposed, mostly implying architectures with several redundancy levels of different actuator's components [12, 13, 14]. These "jam-tolerant" solutions lead to the increase of the number of components and, consequently, to the increase of the overall weight and a significant reduction of the overall reliability, hence increasing the probability of fault occurrence during service [11].

An innovative solution is to employ a simple architecture with the minimum number of needed components, coupled with a prognostic and health monitoring (PHM) system [11, 15, 16]. This would allow to move from a preventive to a condition-based maintenance and potentially to predict the development of a jam-causing degradation, hence removing the need of encumbering mechanical redundancies [17].

To do so, it is of primary importance to have a high-fidelity detailed dynamic model of the various EMA subcomponents, to be used as a virtual test bench on which to inject artificial defects, identify the appropriate feature and verify the PHM approach feasibility. Several researches in literature have highlighted the need to accurately model the mechanical components of EMAs, since they are involved with friction, which is considered the major cause of jamming in EMAs [18, 19, 20, 21]. From the FMECA in [16, 21] it results that the ball screw is among the most critical components in EMAs.

The closed system nature of this components makes it hard to experimentally investigate the behaviour of internal components, therefore several studies have been carried out in literature to analytically investigate the motion of the spheres within the ball screw and the overall efficiency of this mechanism [22]. It is known that the friction torque generated in a ball screw depends on the applied load and how it is redistributed among the different spheres. Yoshida et al. [23] analysed the ball motion and the load distribution in a double nut BS with external recirculation and circular groove, proposing an axisymmetric arrangement of recirculation tubes with regards to the screw axis to compensate for the mass disequilibrium. The load distribution is affected also by elastic deformations and the coupling between deformation modes [24, 25, 26], and thermal decompression due to frictional heating. In fact, the first turns of spheres close to the force application point bear most of the load due to elastic deformation of the structure and, hence, develop more heat by friction: this leads to a partial release of tension for thermal expansion of the first rows of spheres and a partial redistribution of the load on the following rows [27, 28]. The ratio between the external force and the preload should not exceed 2.83 in order to avoid the decompression of the sphere of one of the two nuts, which would cause vibrations, impacts and excessive wear, as found by Wei et al. [29, 30]. Wear is a natural phenomenon that happens naturally with the mechanism's ageing. Nevertheless, several factors can accelerate this process, such as excessive speed, too high preload values, overloads [31], entrance of contaminants or moisture, insufficient or inadequate lubrication and so forth. A theoretical approach to the wear of ball screws was introduced by Wei et al. [22], who performed a quasi-static analysis under the assumption of equally loaded spheres and dry contact conditions, evaluating the wear through an accuracy degradation parameter and a micro-contact

2

asperity model, representing the axial displacement loss due to wear. Experimental data of prolonged wear test on a not preloaded ball screw were obtained by Zhou et al. [32], who proposed also a quasi-static theoretical model, assuming a major wear area and defining a the precision loss rate as the ratio between the total worn volume and the total contact area. A complex wear model, based on multi-scale contact mechanics, was established by Liu et al. [33], basing on a fractal description of the surface and considering the elastic-plastic deformation of each single asperity. Other studies on wear degradation have been performed by Cheng et al. [34] exploiting the kinematic analysis of previous studies [29, 35] to obtain the sliding speed: they applied a modified Archard wear theory to obtain the wear depth and estimate the preload degradation in time. The first effect of wear is the preload lessening, increase of vibration level and stiffness and positioning accuracy reduction. For this reason several studies have been carried out to develop preload monitoring techniques [36, 37, 38] and to accurately describe the influence of the wear rate on the preload degradation [39]. The interested reader can find an exhaustive review in [40].

In this framework, the authors developed a lumped parameter dynamic model of a double-nut preloaded ball screw in [41, 42, 43] which evolved in a more detailed three-dimensional multibody dynamic (MBD) model [44], capable to dynamically describe the motion of all the components of the ball screw mechanism, including each internal spheres, with time variant inputs, disturbances and environmental conditions. The focus has been put on the punctual contact between the spheres and the grooves, considering the presence of grease lubrication. Various fault evolution models have been inserted as well to investigate their influence on the overall behaviour of the mechanism.

In this paper, this model has been used to study the steady-state friction torque which inevitably creates when a non-null speed command is imposed, due to the multiple rolling contacts of the spheres and the grooves and the friction forces generated in the lubricant film. This dissipative effect is commonly evaluated measuring the so called *no-load drag torque* which, according to ISO 3408:1-2006 [45], is defined as the "torque required to rotate the preloaded ball nut relative to the ball screw shaft, or vice versa, in the absence of an external load and any friction torque of the end seals" and support bearings.

The no-load drag torque level supplies different kinds of information. First of all, it indicates the minimum amount of torque which it is required to apply to the rotating part, which in the contest of the current analysis is considered to be the screw shaft, to produce a displacement of the translating part, in this case the nut assembly. This information, together with the friction torque level generated by the bearings and other component of the EMA, is needed in the design phase to select the correct power required for the electric motor to overcome the frictional effects and guarantee the required performance for the designated application [46, 47].

In addition, a preload is commonly applied to compensate for the backlash, provide the required stiffness for dynamic processes and improve the positioning accuracy. Measuring the no-load drag torque helps in the setup of the preload level, which must be decided according to the application: indeed, a low preload might be cancelled by the operative external force restoring the axial play, while a too high value would increase the friction torque and cause overheating for high speed conditions, which in turns would affect the positioning accuracy

3

and the life of the component [48, 49].

Verl and Frey [48] experimentally investigated the drag torque generated in a double nut ball screw varying the static level of pretension and the speed in order to obtain a corrected formula for the estimation of the effective equivalent load to be used in the design phase. They developed a custom test bench, approach which is not applicable in the common practice. For this reason, ball screw manufacturers provide in the catalogues simplified formulae to estimate the no-load drag torque as a function of only the preload, disregarding other parameters such as the type of preload and the internal geometry.

An improved formulation, taking into account the helix and contact angles, friction coefficient, ball diameter, sliding direction and normal contact forces, has been proposed by Zhou et al. [50]. They experimentally studied the link between the drag torque and the preload level with an adjustable preload double nut ball screw at different nut positions along the permissible stroke. The new formulation was found to be more precise than the one usually present in literature.

Both the literature's and Zhou's formulations involve that the drag torque measurement must be executed at 100 [rpm], according to the ISO 3408:1-2006 prescriptions, and no mention to the environmental temperature is given. This procedure implies that the friction torque estimation obtained by the application of both formulation does not represent condition in non nominal situations, such as at different temperatures. In fact, for what concerns flight control EMAs, the operating temperatures are much lower than those commonly present in a manufacturing plants: while the environmental temperature at the standard cruise altitude for commercial aircraft is around $-50\,°\mathrm{C}$, the thermal dissipations within the EMA coming from the different components make the internal temperature to remain higher, albeit below $0\,°\mathrm{C}$. Furthermore, selecting different types and natures of the lubricant can cause the friction torque to vary from the nominal value predicted analytically.

In this paper, the impact of low temperatures on the no-load drag torque of a double nut preloaded ball screw with lubrication is analysed for different preload levels and speeds. Being the previously introduced high-fidelity model used, a physical interpretation of the phenomena affecting the friction level is given as support to the simulation results. In the results and discussion sections it is shown how the no-load drag torque depends on several parameters in addition to the preload.

2. Materials and Methods

The mathematical model [44, 40] used in this paper has been created in the Simscape Multibody environment, which allows to describe the bodies with an acausal object-oriented programming language, which automatically formulates the underlying dynamic equations basing on the interconnections between blocks. The way the various blocks are connected reflects the real world interactions and allows the model design to start from the real structure of the physical system.

The full dynamics of each component is automatically taken into consideration, including gyroscopic and inertial effects. Therefore, the focus has been placed on the development of

the three-dimensional contact model to describe the interactions of each sphere with the grooves and adjacent spheres [51].

Currently, the model does not contemplate the presence of the recirculation path, therefore the model considers an endless helical path composed by the two grooves, in which the spheres continuously move: this obviously involves that, after a certain angle of rotation of the screw shaft, they come out from the nut body and continue to roll in the virtual helix. This situation can also be imagined as a BS with an infinitely long nut. This assumption does not create any issue for what concerns the friction and efficiency values as well as the motion of the spheres and the contact forces. Instead, the reaction forces and torques on the ground and the acceleration spikes of the screw and the nut are affected by this hypothesis. For what concerns the aim of the current research, this issue can be disregarded since only the number of sphere that effectively bear the load are simulated for each nut, ignoring the spheres which lay in the recirculation channel.

A rotating screw and a translating nut have been considered, but this model allows every possible combination to be simulated, such as rotating nut and translating screw or even fixed screw with rotating and translating nut or vice versa. The friction of the screw shaft bearings and the anti-rotation guides of the nut are assumed to be nil in order to study only the ball screw internal contributions. The inertial and geometrical properties of the bodies are retrieved from a 3D CAD model of the ball screw component, developed by the authors.

In this section, the contact model is recalled and thoroughly explained, disregarding the sub-models which, although present, have not been used in the current analysis, such as the degradation models [40]. First, the model topology is introduced; after, the Hertzian normal contact model and the lubrication friction model are presented.

2.1. Ball screw geometry

Independently on how both the screw and the nuts are constrained to the global fixed frame (also known as *ground*), all the spheres preserve their six degrees of freedom and their motion is defined uniquely by the fact to be trapped between the helical grooves: hence, their motion depends on the contact forces with the raceways.

Each body is considered rigid, therefore its positioning and orientation can be described by only one coordinate system (CS). Considering a right-handed threaded ball screw, to describe the position of the screw shaft and of a generic sphere, the three main usual coordinate systems $Ox'y'z'$, $Oxyz$ and $Btnb$ are introduced [40, 35], shown in Fig. 1, which correspond respectively to the global fixed CS, the screw shaft CS centred in O and the Frenet-Serret CS centred in B.

The rotation matrices linking these CSs can be easily constructed referring to Fig. 1 and can be found in [40]. In particular, $\mathbf{T}_{BO}$ is the rotation matrix to transform a vector expressed in the $Oxyz$ CS in the Frenet-Serret CS.

Observing a section normal to the thread, i.e. on a plane containing the n and b axes, the gothic arch profile of the grooves can be identified. Each of the two raceways of the screw shaft and the nut is composed by two half grooves, as shown in Fig. 5, namely S1 and S2 for the screw and N1 and N2 for the nut. The curvature centres of the four half grooves
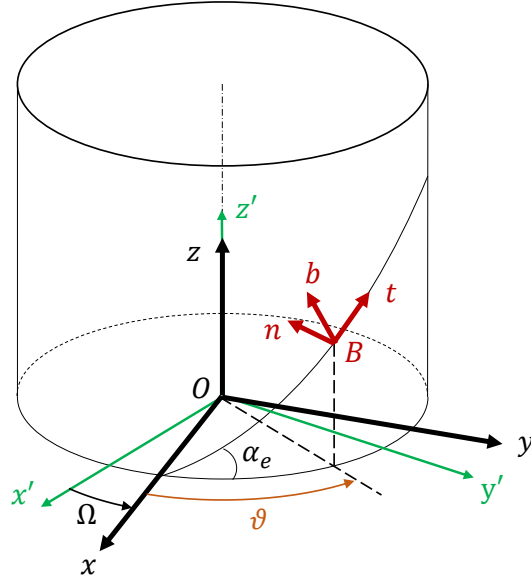
Figure 1: Ball screw's main reference systems.

are C_{1s}, C_{2s}, C_{1n} and C_{2n}, where the subscripts refer to the half grooves names. The shape of the profile is determined by the centre radius offset H and the ogival offset L (Fig. 2).

The procedure detailed hereinafter is applied to each simulated sphere. Only the formulation relative to the half groove S1 is presented to not weigh the dissertation down; those for S2, N1 and N2 can be easily deduced following the same procedure. The three-dimensional contact problem can be reduced to a bidimensional one on the the $n - b$ plane normal to the thread, under the hypothesis of a sufficiently smooth surface of the groove. In fact, if the minimum local curvature radius of the groove is greater than the ball radius, the sphere is always in contact with only one point for each half groove. In particular, if the ideal geometry is assumed, the location of a generic point P, belonging to S1, can be expressed with respect to the Frenet-Serret CS's centre B as:

$$\mathbf{R}^O_{P/B} = [-H + r_s \cos(\alpha_{S1})]\widehat{\mathbf{n}} + [L - r_s \sin(\alpha_{S1})]\widehat{\mathbf{b}} \tag{1}$$

where r_s is the groove radius and α_{S1} the contact angle of the sphere with S1. The latter is defined as the angle between the n axis and the segment connecting the curvature centre C_{1s} and the centre F of the sphere, as can be seen in Fig. 2. The superscripts represent the CS in which the coordinates are expressed (O for the screw CS, B for the Frenet-Serret CS and F for the CS of the sphere), while the subscripts indicate the analysed and reference points.

At each time step of simulation, the position of the sphere is identified by means of the azimuth angle ϑ, and the corresponding ideal location B of the sphere centre is calculated as:
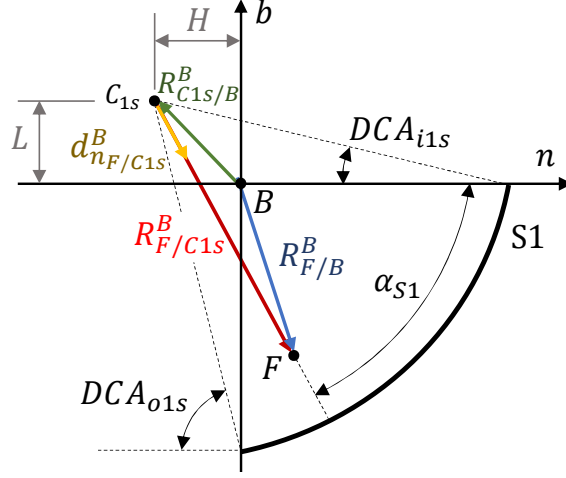
Figure 2: Position vectors on the normal plane.

$$\mathbf{R}_{B/O}^{O} = r_m[\cos(\vartheta) \quad \sin(\vartheta) \quad \vartheta \tan(\alpha_e)]^{T} \tag{2}$$

where r_m is the centre pitch radius and α_e is the helix angle.

In order to uniquely determine the position of the sphere with respect to the screw CS $Oxyz$, it is not possible to get the azimuth angle value from the Simulink built-in *Transform Sensor* block (TS) since it presents a 2π periodicity. However, this blocks gives the relative position and speed of F with respect to O, therefore the continuous azimuth has been calculated as:

$$\vartheta(t) = \int_{t_0}^{t} \frac{x_{F/O}(t)\dot{y}_{F/O}(t) - \dot{x}_{F/O}(t)y_{F/O}(t)}{x_{F/O}^{2}(t) + y_{F/O}^{2}(t)} dt + \vartheta_0 \tag{3}$$

in which ϑ_0 is the initial azimuth angle.

The Transform Sensor block provides also the rotation matrix $\mathbf{T}_{OF}$, which can be used, together with $\mathbf{T}_{BO}$, to obtain the rotation matrix $\mathbf{T}_{BF} = \mathbf{T}_{BO}\mathbf{T}_{OF}$ from the sphere CS (F), which is centred in the sphere centre F and continuously rotates with the progression of the simulation, to the Frenet-Serret CS (B).

In general, F does not coincide with the centre B of the Frenet-Serret CS, which lies on the ideal helix, as depicted in Fig. 2. The relative position can be written as:

$$\mathbf{R}_{F/B}^{B} = \mathbf{T}_{BO}\left(\mathbf{R}_{F/O}^{O} - \mathbf{R}_{B/O}^{O}\right) \tag{4}$$

where $\mathbf{R}_{F/O}^{O}$ is given by the TS block and $\mathbf{R}_{B/O}^{O}$ is defined in Eq. (2).

Since the normal contact force is exchanged along the common normal of the groove and the sphere surfaces, it is important to calculate the versor identifying this direction, as shown in Fig. 2:
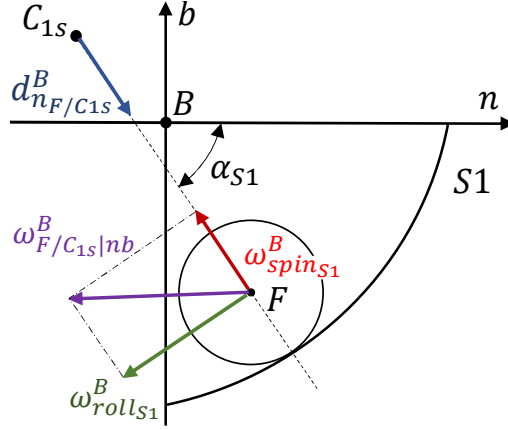
7

Figure 3: Roll and spin velocities of the sphere.

$$\mathbf{d}^{B}_{n_{F/C_{1s}}} = \frac{\mathbf{R}^{B}_{F/C_{1s}}}{|\mathbf{R}^{B}_{F/C_{1s}}|} \tag{5}$$

with

$$\mathbf{R}^{B}_{F/C_{1s}} = \mathbf{R}^{B}_{F/B} - \mathbf{R}^{B}_{C_{1s}/B} \tag{6}$$

where, for S1,

$$\mathbf{R}^{B}_{C_{1s}/B} = -H\widehat{\mathbf{n}} + L\widehat{\mathbf{b}} \tag{7}$$

Consequently, the contact angle can be expressed as:

$$\alpha_{S1} = \arctan\left(\frac{-\mathbf{R}^{B}_{F/C_{1s}} \cdot \widehat{\mathbf{b}}}{\mathbf{R}^{B}_{F/C_{1s}} \cdot \widehat{\mathbf{n}}}\right) \tag{8}$$

Since B belongs to the screw shaft for each time step, and the relative linear and angular speed of F with respect to O, given by the TS block, are the same for each point belonging to the screw shaft body, considering the revolutionary motion of B around $\widehat{\mathbf{z}}$, the following equalities can be formulated:

$$\mathbf{v}^{O}_{F/O} = \mathbf{v}^{O}_{F/B} = \mathbf{v}^{O}_{F/C_i} \qquad \text{i} = 1s, 2s \tag{9}$$

$$\boldsymbol{\omega}^{O}_{F/O} - \boldsymbol{\omega}^{O}_{B/O} = \boldsymbol{\omega}^{O}_{F/B} = \boldsymbol{\omega}^{O}_{F/C_i} \qquad \text{i} = 1s, 2s \tag{10}$$

The translational speed along the common normal $\mathbf{d}^{B}_{n_{F/C_{1s}}}$ results in:

$$\mathbf{v}^{B}_{n_{F/C_{1s}}} = \left(\mathbf{v}^{B}_{F/C_{1s}} \cdot \mathbf{d}^{B}_{n_{F/C_{1s}}}\right) \mathbf{d}^{B}_{n_{F/C_{1s}}} \tag{11}$$

Considering the contact point belonging to the sphere, the tangential speed, which coincides with the slipping speed given Eq. (9), can be calculated as:

8

$$\mathbf{v}^B_{t_{CP_{S1}/C_{1s}}} = \mathbf{v}^B_{t_{CP_{S1}/B}} = \left(\boldsymbol{\omega}^B_{F/C_{1s}} \times (r_b - \delta_{s_{S1}}) \, \mathbf{d}^B_{n_{F/C_{1s}}} \right) +$$
$$+ \mathbf{v}^B_{F/C_{1s}} - \left(\mathbf{v}^B_{CP_{S1}/C_{1s}} \cdot \mathbf{d}^B_{n_{F/C_{1s}}} \right) \mathbf{d}^B_{n_{F/C_{1s}}} \tag{12}$$

where $\delta_{s_{S1}}$ is the contact deformation of the sphere (see section 2.2).

The versor identifying its direction is expressed as:

$$\mathbf{d}^B_t = \frac{\mathbf{v}^B_{t_{CP_{S1}/B}}}{|\mathbf{v}^B_{t_{CP_{S1}/B}}|} \tag{13}$$

The spin velocity of the sphere is oriented along the common normal and positive if coming out from the groove, as shown in Fig. 3:

$$\boldsymbol{\omega}^B_{spin_{S1}} = -\boldsymbol{\omega}^B_{F/C_{1s}} \cdot \mathbf{d}^B_{n_{F/C_{1s}}} \tag{14}$$

The rolling speed is the angular speed vector perpendicular to the common normal and lying on the $n - b$ plane:

$$\boldsymbol{\omega}^B_{roll_{S1}} = -\frac{1}{r_b} \mathbf{v}^B_{CP_{S1}/F} \times \mathbf{d}^B_{n_{F/C_{1s}}} \tag{15}$$

where $\mathbf{v}^B_{CP_{S1}/F}$ is the component directed along t of the peripheral speed of the sphere in the contact point CP_{S1}:

$$\mathbf{v}^B_{t_{CP_{S1}/F}} = \left(\boldsymbol{\omega}^B_{F/C_{1s}} \times (r_b - \delta_{s_{S1}}) \, \mathbf{d}^B_{n_{F/C_{1s}}} \right) \cdot \widehat{\mathbf{t}} \tag{16}$$

2.2. Normal contact model

When the sphere enters in contact with the considered half groove, the normal force is exchanged between the common normal in the contact point. The direction is identified by the versor defined in Eq. (5) and the magnitude is calculated starting from the rigid bodies interpenetration δ_{S1}, as depicted in Fig. 4:

$$\delta_{S1} = |\mathbf{R}^B_{F/C_{1s}}| + r_b - r_s \geq 0 \tag{17}$$

where r_b is the radius of the sphere.

The normal force is composed by an elastic and a damping component; the latter is dynamically saturated to the elastic component value to avoid unrealistic discontinuities and attractive forces due to non-null impact speeds [43]:

$$F_{n_{S1}} = K_H \delta_{S1}^{\frac{3}{2}} + \min \left(C_H |\dot{\delta}_{S1}|, \ K_H \delta_{S1}^{\frac{3}{2}} \right) \text{sign} \left(\dot{\delta}_{S1} \right) \tag{18}$$

The formulation of Antoine et al. [52] of the Hertzian normal problem has been adopted since its explicit non recursive structure is particularly suitable to be inserted into a dynamic model. The so calculated contact stiffness K_H is not a constant value but it varies with the
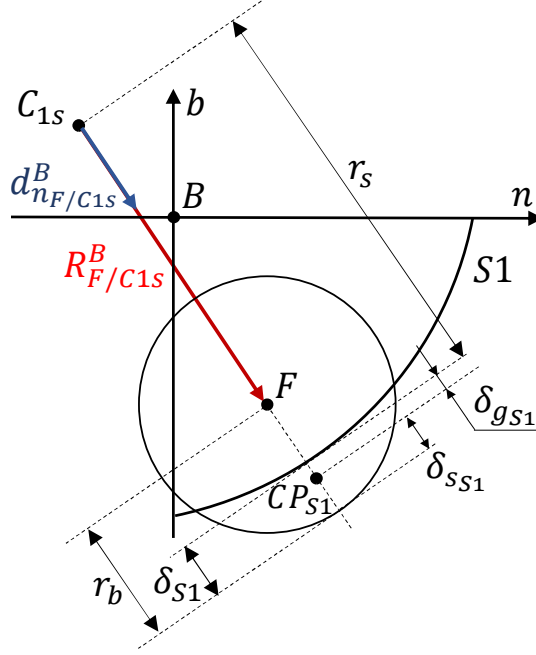
Figure 4: Contact interpenetration and contact point location.

contact angle since the groove first principal curvature depends on it. In order to shorten the simulation time, the stiffness values have been pre-computed and inserted into the model as a bidimensional map, function of the contact angle.

The hysteresis damping coefficient C_H has been assumed to vary with the contact stiffness thereby maintaining a constant value for the damping ratio:

$$C_H = b_h \sqrt{K_H} \tag{19}$$

where b_h is a proportionality coefficient.

Because of the possible use of different materials for the spheres and the grooves, the total deformation has been decomposed in two contributions associated to the two mating bodies, as shown in Fig. 4:

$$\delta_{S1} = \delta_{s_{S1}} + \delta_{g_{S1}} \tag{20}$$

with

$$\frac{\delta_{g_{S1}}}{\delta_{s_{S1}}} = \frac{\left(1 - \nu_g^2\right) E_s}{\left(1 - \nu_s^2\right) E_g} \tag{21}$$

where E and ν represent respectively the Young and Poisson moduli.

In Fig. 5 the gothic profile of both raceways is shown and the four half grooves are depicted. The contact of the sphere with each half groove can occur only if the centre F of the sphere lies within the correspondent "activation area", highlighted with different colours in Fig. 5. Considering now S1, the contact existence conditions are written as:
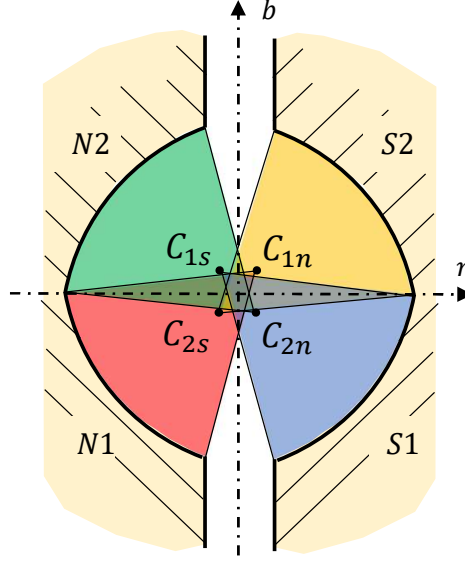
10

Figure 5: Gothic arch profile with half grooves contact activation areas.

$$\begin{cases} DCA_{i1s} \leq \alpha_{S1} \leq DCA_{o1s} \\ |\mathbf{R}_{F/C_{1s}}^{B}| \geq r_s - r_b \\ \mathbf{R}_{F/C_{1s}}^{B} \cdot \hat{\mathbf{n}} \geq 0 \end{cases} \tag{22}$$

where the first row determines the contact angle extremities, defined through the inner and outer design containment angles (DCA) represented in Fig. 2, and the second condition defines the inner contact between two spheres. To avoid an unreal "mathematical contact" of the sphere with the other side of the half groove circumference, the third condition has been added.

This approach allows to represent only one contact point with each half groove, but simultaneous contact with more than one half groove can occur, up to four contacts with all of them in case of preloading with oversized spheres.

2.3. Lubricated friction model

In ball screws the sliding friction is replaced with rolling friction but a little amount of slip always occurs, due to the elastic deformations of the bodies in the contact area and to the kinematics of the mechanism itself. If no lubricant were present, the slip would produce wear on the rolling surfaces and fatigue damage, shortening the life of the component. To avoid this condition a film of lubricant is interposed between the contacting bodies to separate them thanks to the hydrodynamic pressure generated within the lubricant, minimizing wear and friction.

In many machine components lubrication is performed with grease: it is generally composed by a thickening matrix in the form of fibres dispersed inside a base oil. This structure causes a greater friction and temperature rise in the initial churning phase, after which the

11

grease distributes on the raceway's shoulders performing a sealing action against the entrance of external contaminants and creating reservoirs, which, under the effect of shear, capillary and centrifugal forces, replenish the contact with base oil.

Due to this bleeding characteristic of greases, the lubricant layer in the contact track is mainly composed by base oil and a very thin layer of broken thickener fibres from the churning phase. Hence, a simplified elasto-hydrodynamic lubrication model has been developed in [40, 44] considering the base oil as lubrication media and the presence of a permanent layer of residual thickener fibres from the churning phase, which is usually in the order of few nanometres [53].

The lubrication model assumes that the prevalent motion of the spheres is along the t axis, therefore, referring to Eqns. (9) and (15), the entrainment speed can be obtained as the average speed of the two contacting surfaces as:

$$\mathbf{u}_{S1}^B = \frac{1}{2}\left(\mathbf{v}_{t_{CP_{S1}/F}}^B + \mathbf{v}_{F/C_{1s}}^B \cdot \widehat{\mathbf{t}}\right) \tag{23}$$

The flowchart shown in Fig. 6 explains the various tasks computed by the model at each time step. It is a simplified version of that in [40] since no lubricant degradations are considered here.

As can be seen, at each simulation step the dynamic equilibrium equations, solved at the previous time step, provide the relevant kinematic values such as positions and speeds. These quantities are first used to solve the Hertzian normal contact.

Successively, the friction model is solved. Initially, the physical properties of the lubricant within the contact footprint are updated basing on the pressure and temperature. For the time being, the latter is considered constant for all the contact points and the components within the mechanism and it is imposed a priori before the beginning of the simulation, since the thermal model is not developed yet. However, given the temperature, thermal deformations of the bodies are taken into account influencing the geometrical dimensions [40].

The viscosity variation with pressure and temperature has been represented with the Roelands' model [53]:

$$\eta(p, T) = \eta_0 e^{[\ln \eta_0 + 9.67]\left\{\left(\frac{T-138}{T_0-138}\right)^{-S_0}\left(1+5.1\times10^{-9}p\right)^{Z_0}-1\right\}}$$
$$Z_0 = \frac{\alpha_{pv}}{5.1 \times 10^{-9}\left(\ln \eta_0 + 9.67\right)} \tag{24}$$
$$S_0 = \frac{\beta(T_0 - 138)}{\left(\ln \eta_0 + 9.67\right)}$$

where α_{pv} and β are respectively the viscosity-pressure and viscosity-temperature coefficients, η_0 is the reference viscosity at atmospheric pressure and reference temperature T_0.

The density dependence on pressure and temperature has been formulated by means of the Dowson and Higginson formula [53]:
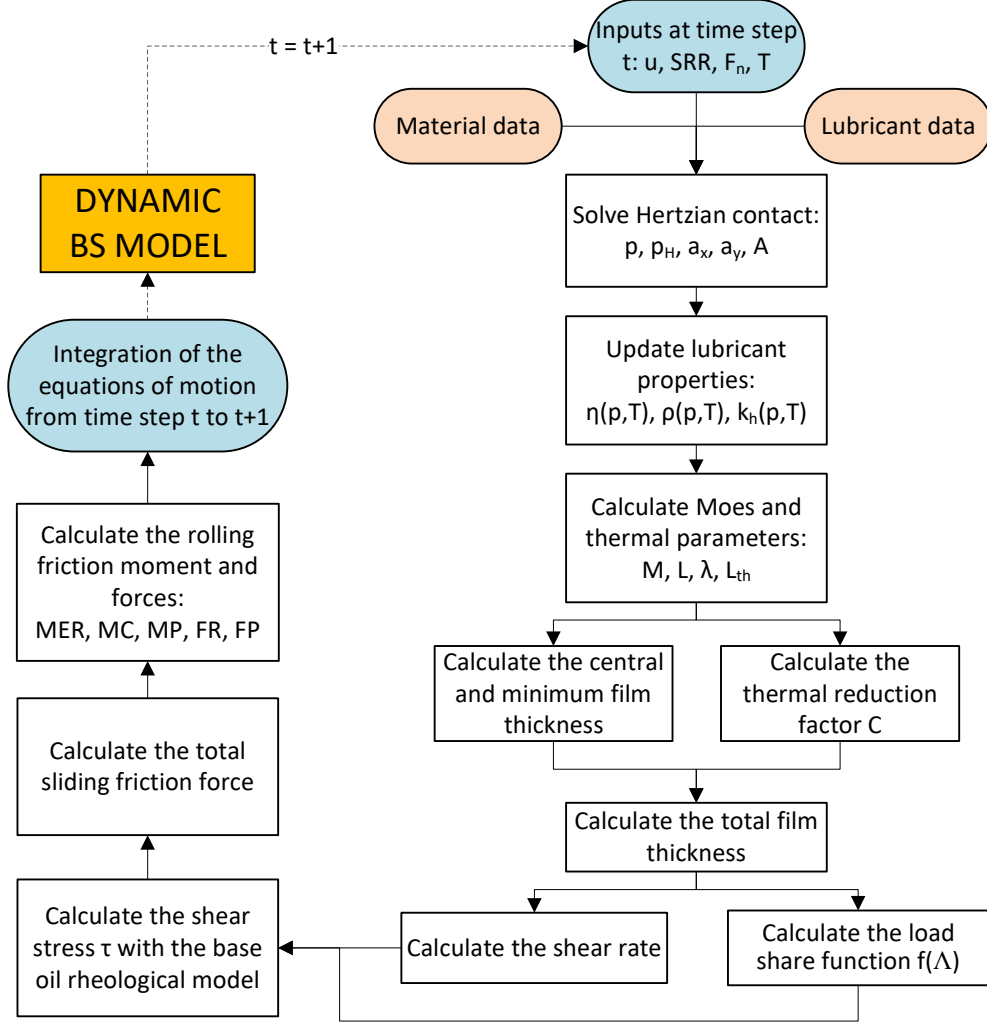
Figure 6: Lubrication model flowchart inside a complete simulation loop.

$$\rho(p, T) = \rho_{T_0} \frac{0.59 \times 10^9 + 1.34p}{0.59 \times 10^9 + p} + \alpha_\rho(T_0 - T) \tag{25}$$

where ρ_{T_0} is the oil density at $T = T_0$ and α_ρ is the density-temperature coefficient.

An important characteristic in the elasto-hydrodynamic lubrication is the film thickness which can be obtained solving the non-linear Reynolds equation together with the elastic half-space and force equilibrium equations [53]. Nijenbanning et al. [54] solved this set of equations repeatedly varying the operative conditions and formulated a fitting equation representing the obtained central film thickness values in all EHL regimes:

$$h_c = R_x \sqrt{2U} \left[\left(H_{RI}^{\frac{3}{2}} + \left(H_{EI}^{-4} + h_{00}^{-4} \right)^{-\frac{3}{8}} \right)^{\frac{2}{3}s} + \left(H_{RP}^{-8} + H_{EP}^{-8} \right)^{-\frac{1}{8}s} \right]^{\frac{1}{s}} \tag{26a}$$

13

$$s = \frac{3}{2} \left(1 + e^{-1.2 \frac{H_{EI}}{H_{RI}}} \right) \tag{26b}$$

$$h_{00} = 1.8 \lambda^{-1} \tag{26c}$$

$$H_{RI} \approx 145 \left(1 + 0.796 \lambda^{\frac{14}{15}} \right)^{-\frac{15}{7}} \lambda^{-1} M^{-2} \tag{26d}$$

$$H_{RP} = 1.29 (1 + 0.691\lambda)^{-\frac{2}{3}} L^{\frac{2}{3}} \tag{26e}$$

$$H_{EI} = 3.18 \left(1 + 0.006 \ln(\lambda) + 0.63 \lambda^{\frac{4}{7}} \right)^{-\frac{14}{25}} \lambda^{-\frac{1}{15}} M^{-\frac{2}{15}} \tag{26f}$$

$$H_{EP} = 1.48 \left(1 + 0.006 \ln(\lambda) + 0.63 \lambda^{\frac{4}{7}} \right)^{-\frac{7}{20}} \lambda^{-\frac{1}{24}} M^{-\frac{1}{12}} L^{\frac{3}{4}} \tag{26g}$$

where M, L and λ are the Moes' dimensionless groups [54] defined as

$$M = \frac{F_n}{E^* R_x^2} \left(\frac{E^* R_x}{\eta_{0T} u} \right)^{\frac{3}{4}} \tag{27}$$

$$L = \alpha_{pv} E^* \left(\frac{E^* R_x}{\eta_{0T} u} \right)^{-\frac{1}{4}} \tag{28}$$

$$\lambda = \frac{R_x}{R_y} \tag{29}$$

in which R_x and R_y are the reduced curvature radii respectively in the x direction, coincident with the t axis, and on the transverse y direction, perpendicular to x, $E^* = 2E_h^*$, u is the magnitude of $\mathbf{u}_{S1}^B$ defined in Eq. (23) and η_{0T} is the base oil dynamic viscosity at atmospheric pressure and at the oil operating temperature T.

The minimum film thickness can be approximated by [53, 55]:

$$h_0 = \frac{3}{4} h_c \tag{30}$$

The local heat generated by lubricant shearing in the inlet zone due to back flow induces a film thickness reduction. The ratio between the actual and the isothermal film thickness was formulated by Gupta et al. [56]:

$$C = \frac{1 - 13.2 p_h E^{*-1} L_{th}^{0.42}}{1 + 0.213(1 + 2.23 SRR^{0.83}) L_{th}^{0.64}} \tag{31}$$

where SRR is the slide to roll ratio, p_h is the maximum Hertzian pressure and L_{th} is an additional dimensionless parameter:

$$L_{th} = \frac{\eta_{0T} \beta u^2}{k_h} \tag{32}$$

where $k_h = k_h(p, T)$ is the thermal conductivity of the lubricant, dependent on pressure and temperature [53].

14

Eventually, considering the layer of broken fibres with thickness h_R, the total central film thickness can be calculated as:

$$h_{Tc} = Ch_c + h_R \tag{33}$$

Similarly to the Grubin's theory [53], a simplification can be used considering a uniform film thickness inside the EHL contact. Furthermore, friction is simply estimated from Couette shear of a lubricant film between parallel surfaces, having Hertzian diameter and pressure profile.

Therefore, considering Eq. (12), the lubricant shear rate can be approximated, assuming the velocity as a continuous function across the film with no-slip conditions at the interfaces, as:

$$\dot{\gamma} = \frac{\partial u}{\partial h} \approx \frac{|\mathbf{v}^B_{t_{CP_{S1}/C_{1s}}}|}{h_{Tc}} \tag{34}$$

Thus, the average shear stress within the lubricant film can be obtained with the choice of a lubricant rheological model. In this paper, the widespread Eyring model has been adopted [53]:

$$\tau = \tau_e \arcsin\left(\frac{\eta(p,T)\dot{\gamma}}{\tau_e}\right) \tag{35}$$

where τ_e is the Eyring stress, namely the stress at which the fluid's behaviour starts to be non linear.

The total sliding friction force is then:

$$F_t = \tau A \left(1 - f(\Lambda)\right) + f(\Lambda)\mu_{dry}F_n \tag{36}$$

where A is the Hertzian contact area, μ_{dry} is the dry coefficient of friction and $f(\Lambda)$ is the load share function [57, 58], defined as the ratio between the load F_{n_a} borne by the asperities in direct contact and the total normal force:

$$f(\Lambda) = \frac{F_{n_a}}{F_n} = 1 - \frac{1.2\Lambda^{0.64}}{1 + 0.37\Lambda^{1.26}} \tag{37}$$

Therefore, the friction force is a non linear weighted sum of the complete dry and lubricated contributions, depending on the Tallian parameter Λ [59], which expresses the ratio between the film thickness and the composite surface roughness allowing to describe a continuous transition between boundary, mixed and full film lubrication regimes:

$$\Lambda = \frac{h_{Tc}}{\sqrt{\sigma_1^2 + \sigma_2^2}} \tag{38}$$

with σ_1 and σ_2 the RMS roughness of the two surfaces.

According to Olaru et al. [60] in ball screws two main regimes can occur: the isoviscous-rigid (IVR) and the elasto-hydrodynamic (EHL). The hydrodynamic rolling resistance force

FR due to Poiseuille flow of the lubricant can be expressed as a combination of the values obtained in these two regimes, as:

$$FR_{IVR} = 2.9766 E^* R_x^2 \lambda^{-0.3316} W^{\frac{1}{3}} U^{\frac{2}{3}} \tag{39}$$

$$FR_{EHL} = 7.5826 E^* R_x^2 \lambda^{-0.4055} W^{\frac{1}{3}} U^{\frac{3}{4}} \tag{40}$$

$$FR = \frac{FR_{IVR} - FR_{EHL}}{1 + 0.0841 \lambda^{0.6029} W U^{-0.75}} + FR_{EHL} \tag{41}$$

where $W = ML^3 \left(\alpha_{pv} E^*\right)^{-3}$ and $U = 0.5L^4 \left(\alpha_{pv} E^*\right)^{-4}$ [53].

The component FP of the lubricant pressure in the contact inlet zone directed along the rolling direction can be related to FR as [61]:

$$FP = 2FR \frac{R_x}{R_x + r_b} \tag{42}$$

In addition, Balan et al. [62, 63] formulated an approximated relationship for the rolling resistant moment around the contact footprint centre caused by rolling elastic hysteresis losses and contact micro-slips:

$$MER = 7.48 \times 10^{-7} r_b^{0.33} F_n^{1.33} \left[1 - 3.519 \times 10^{-3} (\lambda^{-1} - 1)^{0.8063}\right] \frac{\mu_s}{\mu_{dry}} \tag{43}$$

where $\mu_s = F_t/F_n$ is the equivalent sliding coefficient of friction.

The race curvature in space originates additional micro-slip and a consequent supplementary resistant moment MC [62]:

$$MC = 0.0806 \mu_s \frac{F_n a_y^2}{2R_y} \tag{44}$$

where a_y is the contact footprint dimension in the y axis transverse to the direction of motion.

Finally, the spin motion of the sphere is hindered by the spinning torque MP [63]:

$$MP \cong \left[\frac{3}{8} + \left(\frac{3\pi}{16} - \frac{3}{8}\right) \kappa^{-0.945 - 0.016 \ln(\kappa)}\right] \mu_s F_n a_y \tag{45}$$

with $\kappa = \frac{a_x}{a_y}$ the ellipticity ratio between the minor and major contact ellipse half widths.

2.4. Forces and moments projection

The contact area is extended along the y direction, therefore the main motion of the lubricant trough it is along the t axis [64]: hence, it is assumed that FR acts along this direction. It is applied on the groove in the same direction, since it is a braking force created by the hydrodynamic effect [62, 63, 61]. FP is applied on the sphere centre opposing to its translational speed since it is generated by forces normal to the sphere, as shown in Fig. 7.
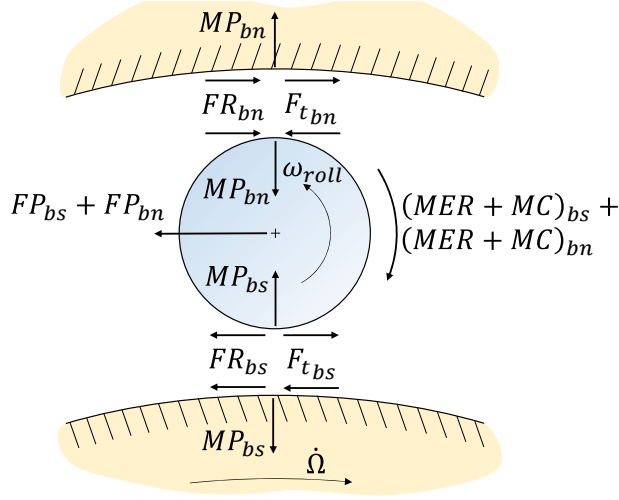
16

Figure 7: Forces direction on the sphere and the screw (lower) and nut (upper) grooves. Forces and moments between adjacent spheres are not represented, although present, to not excessively complicate the figure.

Considering the rotation matrices $\mathbf{T}_{BF}$ and $\mathbf{T}_{OF}$, the calculated normal and friction actions generate forces and moments on the sphere, screw shaft and nut. The force and moment vectors on the sphere with respect to the sphere CS, expressed in the same CS are:

$$\mathbf{F}_{sphere}^{F} = \mathbf{T}_{BF}^{-1} \left[-F_{n_{S1}} \mathbf{d}_{n_{F/C_{1s}}}^{B} - F_{t_{S1}} \mathbf{d}_{t}^{B} + (FP - FR)\,\widehat{\mathbf{t}} \right] \tag{46}$$

$$\mathbf{M}_{sphere}^{F} = \mathbf{T}_{BF}^{-1} \left[(r_b - \delta_{s_{S1}})\,\mathbf{d}_{n_{F/C_{1s}}}^{B} \times \left(-F_{t_{S1}} \mathbf{d}_{t}^{B} - FR\,\widehat{\mathbf{t}} \right) + \right.$$
$$\left. -(MER + MC)\,\mathbf{d}_{\omega_{roll}}^{B} + MP\,\mathbf{d}_{n_{F/C_{1s}}}^{B} \right] \tag{47}$$

while those on the screw shaft with respect to the $Oxyz$ CS, expressed in the same CS can be expressed as:

$$\mathbf{F}_{screw}^{O} = \mathbf{T}_{BO}^{-1} \left[F_{n_{S1}} \mathbf{d}_{n_{F/C_{1s}}}^{B} + F_{t_{S1}} \mathbf{d}_{t}^{B} + (FP - FR)\,\widehat{\mathbf{t}} \right] \tag{48}$$

$$\mathbf{M}_{screw}^{O} = \mathbf{F}_{screw}^{O} \times \mathbf{R}_{CP_{S1}/O}^{O} - \mathbf{T}_2 \left(MP\,\mathbf{d}_{n_{F/C_{1s}}}^{B} \right) \tag{49}$$

where, remembering Eqns. (2), (5) and (7), the position of the contact point CP_{S1} with respect to the screw origin O, expressed in $Oxyz$, can be written as:

$$\mathbf{R}_{CP_{S1}/O}^{O} = \mathbf{T}_{BO}^{-1} \left[(r_s + \delta_{g_{S1}})\,\mathbf{d}_{n_{F/C_{1s}}}^{B} + \mathbf{R}_{C_{1s}/B}^{B} - \frac{MER + MC}{F_{n_{S1}}}\,\widehat{\mathbf{t}} \right] + \mathbf{R}_{B/O}^{O} \tag{50}$$

in which the term involving MER and MC represents the displacement of the centre of the pressure distribution in the direction of rolling.

The sum of the contributions obtained from Eq. (49) for all the spheres of both nuts creates the total friction torque around the screw axis.
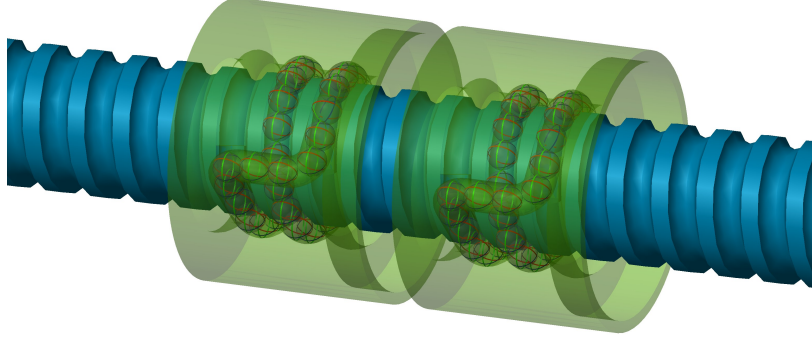
17

Figure 8: Visual representation of the Simscape multibody model.

2.5. Sphere to sphere contact model

The same contact formulation explained in Secs. 2.2 and 2.3 has been applied in the contact between adjacent spheres. However, the computation of the kinematic values, such as the relative speed and position, is easier because of the simple spherical geometry of both contacting bodies.

3. Results and discussion

The model geometry has been created in Solidworks and imported as Parasolid into Simscape, resulting in the initial configuration shown in Fig. 8. The contact model presented in Sec. 2 is applied to each sphere of the two nuts four times, one for each half groove.

The geometrical parameters of the considered double nut preloaded ball screw are summarized in Tab. A.1. A lithium 12-hydroxystearate-thickened (Li/SS) grease has been considered [53, 55, 65, 66, 67], whose properties are listed in Tab. A.2.

As explained in [44], the ball screw mechanism is speed controlled with a PI scheme using the screw shaft angular speed as feedback. The system is considered in vertical position, with the master nut (Nut 1) above the slave nut (Nut 2).

Several simulations have been performed to obtain the plots presented in this section. For each one, the preload is applied with a smooth step in the first 5 [ms] between the two nuts. Because of the preload and the gravity due to vertical arrangement, an initial settling phase is present, though very short. Once the system has reached the equilibrium, a smooth step speed command is imposed to the screw from 0.05 [s] to 0.1 [s] in order to reach constant speed conditions, which are kept for 0.5 [s]. The various quantities have been extracted from the last 0.2 [s] of simulation. Little variations of the obtained values from the overall trend of the graphs can be present due to possible numerical artefacts, especially at low speeds, and to the averaging process during the considered 0.2 [s]. No external force is applied to the system, therefore no mechanical efficiency values are shown in this paper.

In order to make the figures clearer, only the results regarding one of the sphere of each nut are shown. Different values of preload and speed have been considered, respectively in the ranges $0 \div 3000$ [N] and $100 \div 4000$ [rpm]. The results have been analysed at environmental temperatures of -20, 20 and $60\,^{\circ}$C. For the time being, the temperature is considered

constant throughout the entire duration of each simulation and it is set in advance. Thermal deformations of the screw, nuts and spheres are taken into account depending on the simulation temperature, according to [40]. The investigation of the dynamic capabilities of the current model are out of the scope of this paper: it has been presented and described, together with the Simscape practical implementation, in [44].

The values of the torque requested on the screw shaft to guarantee a constant speed with different preload levels are shown in Fig. 9 for different temperatures. This torque is needed to overcome the frictional effects generated by the contact between the spheres and the grooves: hence, intuitively, the higher the preload, the higher the contact forces and, then, the friction. The manufacturers catalogues give an estimation of the no-load drag torque using the following formula [68]:

$$T_{drag_{lit}} = \frac{K_p p}{2\pi} F_{pr}$$

$$K_p = \frac{1}{\eta_1} - \eta_2 \qquad \eta_1 = \frac{\tan{(\alpha_e)}}{\tan{[\alpha_e + \arctan{(\mu_{lit})}]}} \qquad \eta_2 = \frac{\tan{[\alpha_e - \arctan{(\mu_{lit})}]}}{\tan{(\alpha_e)}} \qquad (51)$$

which describes a linear correlation with the preload force F_{pr}, based on the equivalent coefficient of friction μ_{lit}, assumed equal to 0.002 in Fig. 9, which is consistent with test data for the ball screw considered in this analysis. Sometimes, the proportionality coefficient K_p is approximated as $K_p = 0.05/\sqrt{\tan \alpha_e}$ [69, 70]. The estimated drag torque is shown with the thick black line in Fig. 9.

Recently, Zhou et al. [50] affirmed that the energy conservation principle on which Eq. (51) is based is improperly applied since the preload is an internal force and does not produce any work. Therefore, they expressed the correlation between the preload and no-load drag torque in a new fashion:

$$T_{drag_{Zhou}} = \mu_{lit} F_{pr} \sin{(\alpha_0)} [r_m + r_b \cos{(\alpha_0)}] \cos^2{(\alpha_e)} \qquad (52)$$

where α_0 is the nominal contact angle, equal to 45°. The updated drag torque estimate is shown with the dashed black line in Fig. 9.

The prediction of the no-load drag torque obtained from Eq. (52) is lower than that coming from Eq. (51) and it was validated experimentally by the authors. The new formula takes into account more parameters, such as the contact angle, various geometrical dimensions, the normal contact force and the prevalent sliding direction [50], the last two not explicitly visible in the formula but used during its derivation. Both expressions refer to an angular screw shaft speed of 100 [rpm], according to the prescription of the ISO3408-3:2006 standard [71].

However, these relationships represent almost static conditions and no links are given for what concerns speed and temperature variations. In Fig. 9 the results obtained from the model are shown for different temperatures, already cleaned from the torque component due to gravity, showing, as predicted, a linear behaviour. It can be seen that, while for 20 °C and 60 °C the no-load drag torque values match with the outcomes of Eq. (52), the same
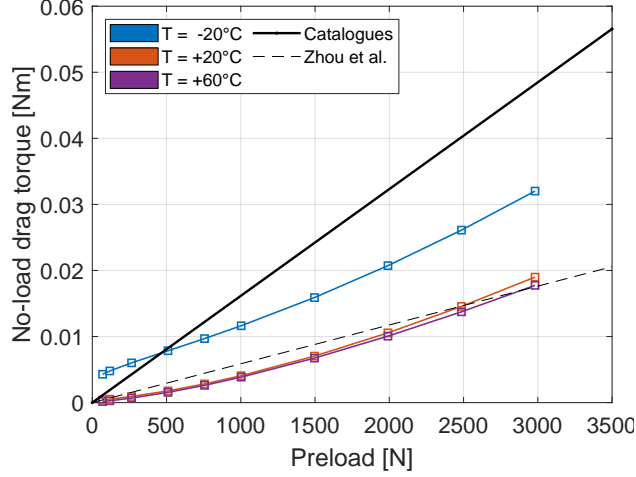
Figure 9: No-load drag torque at 100 [rpm] for different temperatures and comparison with literature formulae.

cannot be said of the drag torque generated at $-20\,^{\circ}\text{C}$, which shows also higher values for low preloads. This should be taken into account during the design phase of a machine, such as flight control EMAs, which has to operate in a low temperature environment.

The level of detail of the model described in Sec. 2 allows to investigate the roots of this behaviour analysing the contacts between each individual sphere with the grooves. Independently from the operating temperature, increasing the preload causes the normal contact force between spheres and grooves to rise, as shown in Fig. 10a. It can be noted that the forces relative to the spheres in the master nut are slightly lower than those of the slave nut, due to the weight of the nuts themselves, which weigh on the lower nut. The contact forces generated in the contact of the spheres with both screw and nut grooves are almost equal, except for the weight of the sphere which gives a negligible contribution. Note that the value of the normal force shown in Fig. 10a refers to a total of 25 simulated spheres per nut: in fact, although the nominal number of sphere for each nut is 30 (Tab. A.1), an average of five spheres are always engaged in the recirculating path, leading to 25 effectively loaded spheres.

Figure 10a shows also the friction forces: they are the major responsible for the friction torque increase. The ratio between these and the normal forces represents the instantaneous friction coefficient, shown in Fig. 11b for different speeds. Its value is considerably small, denoting conditions close to pure rolling, as expected in ball screws, especially at low speeds. Increasing the preload, the normal forces rise more than the friction forces, leading to lower ratios between these quantities (Fig. 11b). As expressed in Eq. (36), the resultant friction force in a contact, as those depicted in Fig. 10a, depends on both the force generated within the lubricant thickness (Fig. 10c) and by the dry direct contact between asperities (Fig. 10d). Analogously to what seen in Fig. 9, higher friction coefficient values arise for low temperatures. It is interesting to note that, for low preloads, the coefficient of friction decreases fast, while as the preload increases its diminishing rate decreases. As the
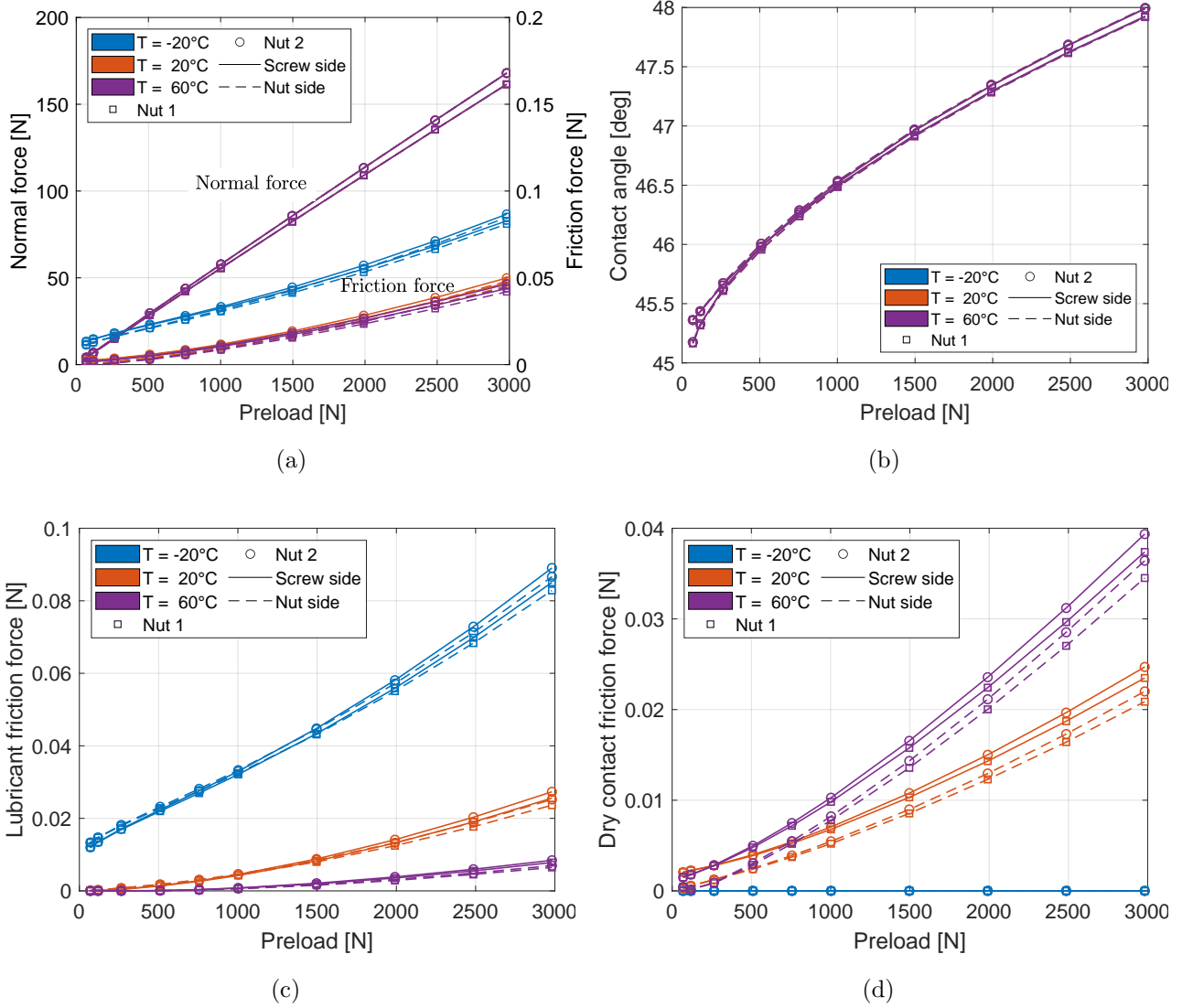
20

Figure 10: Simulation results for one sphere of master nut at 100 [rpm]: (**a**) Normal and friction forces; (**b**) Contact angle; (**c**) Lubricant component of the friction force; (**d**) Direct contact component of the friction force.

temperature decreases, the plateau region is reached at higher preload values.

This can be ascribed to the lubricant viscosity: in fact, according to Roelands' model of Eq. (24), it increases with the normal force and, hence, it grows with the preload. For what concerns the temperature, a big influence of the temperature on the viscosity has been encountered experimentally [53], enclosed in Roelands' model, especially for low temperature. The higher viscosity plays two roles: it has the effect of thicken the lubricant film, as can be seen observing the Tallian parameter in Fig. 10e, and it affects the relationship between the shear rate and the shear stress, expressed in Eq. (35). These two effects are concurrent for
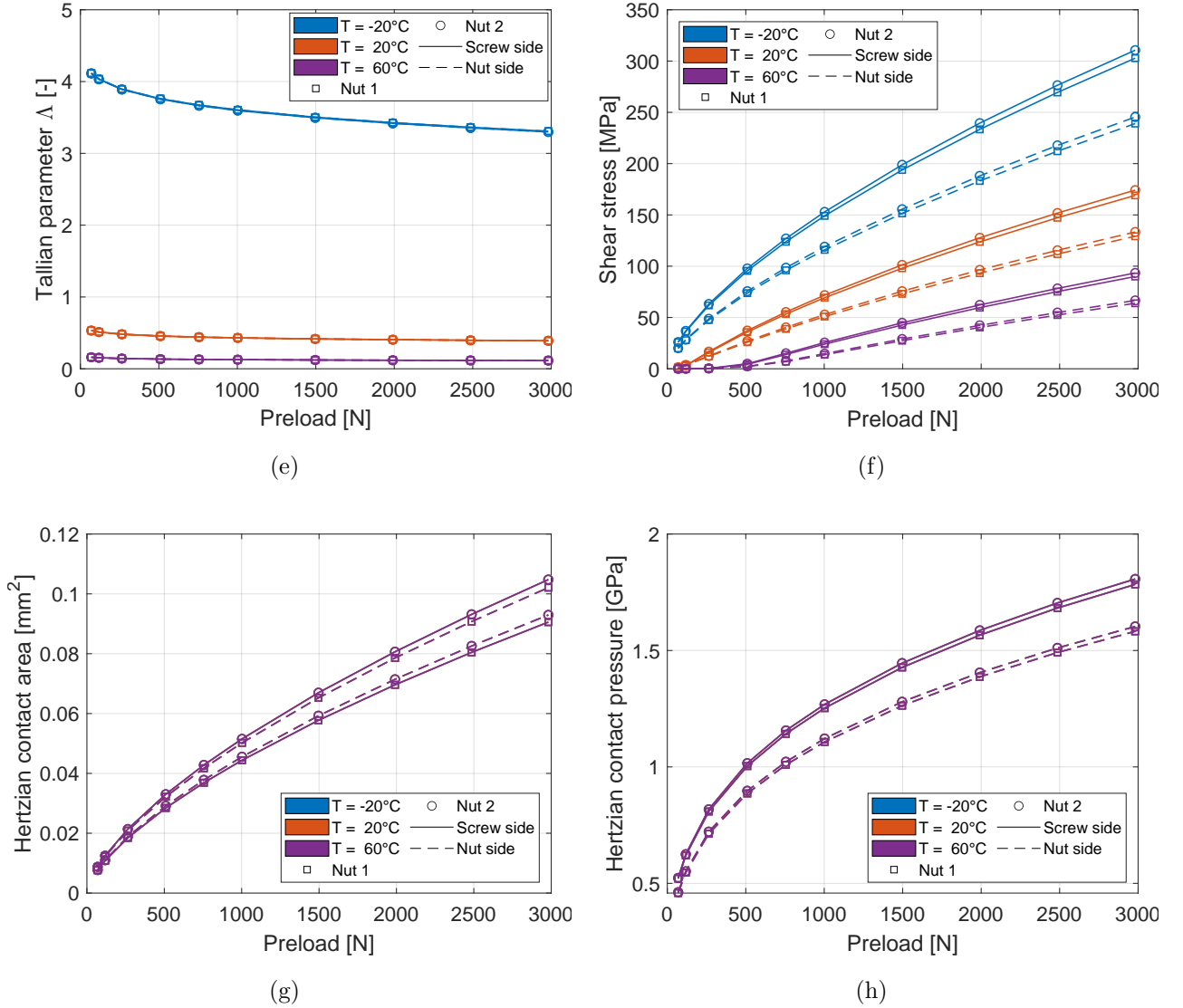
21

Figure 10: Simulation results for one sphere of master nut at 100 [rpm]: (**e**) Tallian parameter; (**f**) Shear stress; (**g**) Hertzian contact area; (**h**) Hertzian contact pressure.

what concerns the shear stress, and hence the lubricant friction force. In fact, considering Eq. (34), a thicker film of lubricant would decrease the shear rate and thus the shear stress, according to the rheological model. On the other hand, the higher viscosity directly affects the shear stress. Looking at Fig. 10f it results obvious that this second phenomenon prevails and the shear stress increases with lowering temperature values.

The lubricant film thickness influences the wear rate of the mating surfaces [53, 40]: the lower the Tallian parameter, the more probable a direct contact of surface asperities and, hence, the more severe the wear. With reference to Eq. (29), a value of the Tallian parameter lower than 2-3 leads the contact to operate in mixed lubrication. In this situation, direct

22

contacts can occur and the friction force is transmitted both by dry asperities contacts and lubricant shearing: the two contributes are detailed in Figs. 10c - 10d. It can be noted that, since at $-20\,°C$ the Tallian parameter is higher than the mixed lubrication threshold, all the friction force is generated by the lubricant shear. At $20\,°C$ the mechanism is operating in mixed lubrication conditions and the total friction force is transmitted together by the lubricant film and dry contacts. At $60\,°C$ the Tallian parameter is even lower, indicating an almost boundary lubrication situation: in fact the force transmitted by the asperities in direct contact is comparable with that obtained by the lubricant film shear. The latter condition should be avoided since it implies high wear rates and a premature failure of the component.

The displacement of the friction coefficient's plateau to higher preload values for decreasing temperatures can be explained observing that the Tallian parameter diminishes with the preload but, at $-20\,°C$, it maintain the contact in full lubrication condition even at the highest preload value: this means that the friction force is almost entirely given by the lubricant shearing and then it is fully influenced by the viscosity increase. Conversely, at higher temperatures, the thinning of the lubricant leads to a friction force more and more governed by dry coefficient of friction, which is much less sensitive to the normal force value and then to the preload.

It is worth to be highlighted that the instantaneous coefficient of friction values arising in the contact area with the screw side are higher than those with the nut grooves (Fig. 10a and 11b) and this is due to the difference in the main curvature of the two grooves [40]. Figure 10h depicts the Hertzian pressure generated at the two contact interfaces: the main curvature radius of the nut grooves is higher and opposite in sign with respect to the screw main curvature radius, leading to a higher contact footprint area (Fig. 10g) and, hence, a smaller contact pressure. The high values of contact pressure are typical of ball screw and similar to those arising in ball bearings [53, 72]. This higher pressure is also the reason why the shear stress within the lubricant layer, depicted in Fig. 10f, is greater in the sphere/screw interface. To this effect contributes also to the fact that the slipping behaviour in the sphere/screw interface is usually greater than that in the sphere/nut contact points, since the screw shaft is the driving element. Since the rolling conditions are close to pure rolling, the slipping speed is very low and, therefore, also the friction force. When the sliding speed is below a certain threshold, usually indicating the speed at which the maximum friction coefficient occurs, the dependence of the friction force from the sliding speed is almost linear, since the friction model is implemented as speed dependent, which means that there must exist a non-null sliding speed, even if extremely small, to create a friction force, as in [43, 73] or as implemented in commercial MBD softwares such as MSC ADAMS. This is required to avoid integration instabilities, such as those that would occur with a pure Coulomb friction model, which would lead to the simulation failure, especially when the components involved in the contact have extremely low mass and inertia, fact that makes them more prone to be affected by spikes in the force acceleration signals. In this case, the sliding speed are well below this threshold and therefore in the linear region: consequently, since in the screw/sphere interface there are a slightly higher slipping speed, the friction forces obtained in this point is greater than those on the nut side. The small

sliding speed obtained in the contacts may also be seen as representative of microslip which generates in the contacts due to the non-punctual contact point.

The friction torque depends on the projection of the contact forces on the nuts and screw shaft, and this is directly dependent on the direction of the contact forces in space, i.e. on the contact angle. Figure 10b represents the variation of this value on both nuts and grooves: the higher the preload, the higher the contact deformations and, hence, the greater the variation of contact angles from the nominal value of 45°.

Hitherto, all the observations have been made upon graphs obtained at an angular screw shaft speed of 100 [rpm], according to ISO3408-3:2006 [71]. However, the operating speed is an important factor to be considered when evaluating friction related quantities, such as the no-load drag torque. Figure 11a depicts this drag torque as a function of the preload level for different speeds and temperature: it is given by all the contributions of all the spheres from the two nuts, as in Fig. 9. Because of the type of lubricant, the 60 °C curve is similar to the 20 °C one in the frame of the current analysis, therefore it has been omitted in Fig. 11 for the seek of plots' clearness.

It can be observed that the speed dependence of the friction torque is more marked for low temperature. In fact, as previously stated, the low temperature friction comes primarily from the shearing of the lubricant film under high viscosity conditions, and the rheology of the lubricant in Eq. (35) describes a shear stress dependence on both viscosity and shear rate, the latter directly influenced by the operating speed. Instead, at higher temperature, the speed effect is less pronounced because of the lower load share function value Λ (Eq. (29)) and due to the lower viscosity of the lubricant. However, even if with different rates, an increase in the operating speed leads to the increase of the friction torque.

The instantaneous friction coefficient curves are depicted in Fig. 11b, from which it can be seen that on the screw side it always creates a slightly higher coefficient of friction because of the higher pressure. No significant differences can be seen between the master and slave nut when no external load is applied. At low speed the lubricant film does not completely build up (as can also be observed from Fig: 10e realized at 100 [rpm]) and the friction is determined mainly by direct contact of asperities. Instead, when the speed augments the surfaces are separated by the lubricant and the friction becomes almost entirely dependent on the film shearing, which, at higher temperature, creates less frictional effects due to the remarkably lower viscosity.

Figure 11c shows the value of the contact angles for different preload levels and screw speeds. In absence of an external force and at low preloads, the sphere are lightly loaded and, therefore, more free to move between the grooves. In fact it is interesting to note that, at low preloads, the contact angles on the screw and nut sides distances from the mid value which they assume for low speeds, in order to equilibrate the centrifugal forces: this effect is more pronounced for higher operating speeds. However, when the preload increases the spheres are more pressed and trapped between the grooves: the centrifugal force becomes negligible with respect to the other contact forces and the contact angles does not vary between the screw and nut side.
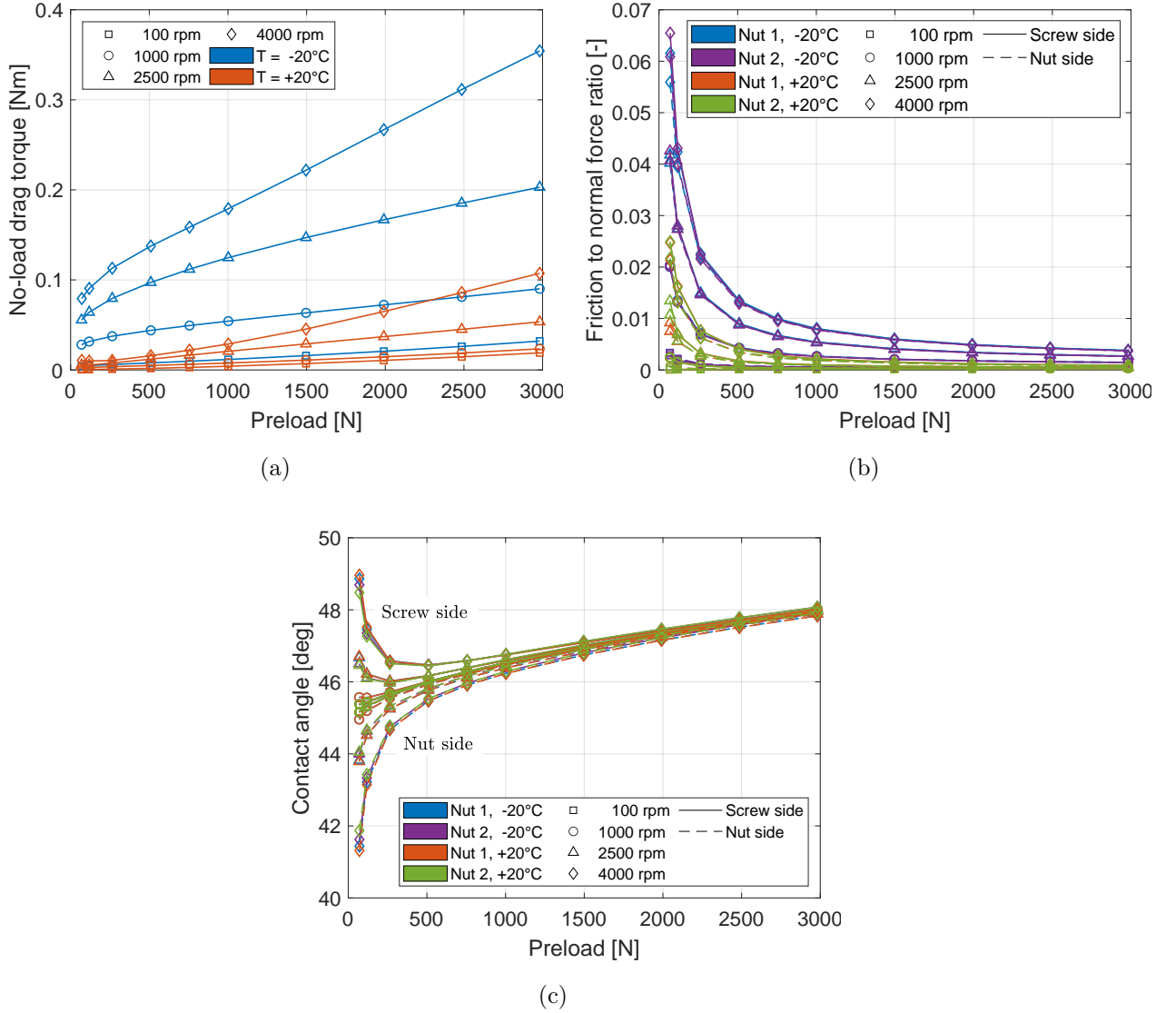
24

Figure 11: Influence of speed on (**a**) the total no-load drag torque generated by all the spheres of both nuts, (**b**) the sliding friction coefficient of single contacts. and (**c**) the contact angles.

4. Conclusions

In this paper the no-load drag torque generated in a ball screw mechanism has been investigated. This quantity is a crucial factor in the design of a ball screw drive system, such as electro-mechanical actuators, since it directly affect the size of the motor and it should be carefully taken into account during the design phase. Usually, manufacturers estimate the friction torque generated in absence of external force applied on the nuts assembly as a linear function of the preload, without considering other geometrical features and parameters, such as speed and temperature. In this research activity, a sensitivity analysis of the no-load drag

torque with respect to the operating angular speed, preload and temperature has been carried out and the results have been interpreted and explained with a physics-based approach.

With this aim, a full MBD mathematical model of a double nut preloaded ball screw has been exploited: it has been thoroughly described together with the details about the representation of lubricated contacts. The model is capable of describing the full dynamics of each subcomponent taking into consideration all their six degrees of freedom and gyroscopic effects. A three-dimensional contact model has been developed to describe the interaction between spheres and gothic arch helical grooves. Sphere to sphere contacts has been considered as well and supports' friction has been disregarded to focus the analysis only on the friction torque component generated internally to the ball screw.

The main results that can be drawn from the current analysis are summarised as follows:

- the no-load drag torque is a linear function of the preload and its variation rate is directly dependent on the operating speed;

- higher operating speeds cause the no-load drag torque to rise and this effect is more pronounced for lower temperature because of the sensibly higher viscosity of the lubricant;

- at lower temperatures the higher viscosity of the lubricant leads to thicker film and then low wear rates but, at the same time, to greater shear stress levels and, hence, increased friction;

- at higher temperatures the lubricant film becomes thinner and the contacts might operate in mixed or even boundary conditions, with greater wear rates;

- at higher temperature the coefficient of friction is lower than that arising in low temperature conditions because of the lower lubricant viscosity and the load share between lubricant film and asperities;

- the friction generated in the sphere/screw interfaces are usually greater than that in the sphere/nut contact points, because of the different Hertzian contact pressures given by the different main curvature radii of the grooves.

- when the ball screw is lightly loaded, either by external force or preload, the contact angles on both the screw and nut sides vary sensibly with the speed increase to compensate the centrifugal force, while at high preloads its effect is negligible.

The specific results obtained in this paper depend on the type of selected lubricant and its physical properties. Different kinds of lubricants exist: some of them are more suited to operate at low temperatures than others and, therefore, they can generate film thicknesses and shear stresses of different values for the same operative and environmental conditions. For example, the lubricant assumed in the current analysis is not suited for high temperature since its decrement of viscosity makes it not capable of guarantee a proper surfaces separation.

In conclusion, the no-load drag torque estimation with literature formulas should be taken with care considering that the calculated value is not only a function of the preload.

With the aim of confirm the lubricant friction model, a three-dimensional multi-physics EHL FEM analysis code is being constructed to compare the results with those of the simplified fast model.

The results of the model presented in this paper have not been experimentally verified yet. In order to validate the model and its results, an experimental test bench of ball screw drives have been designed [74] and it is currently under construction. The primary next goal of the research project will be to investigate the correspondence of these results with experimental trends. In order to measure the no-load drag torque, a torque meter is interposed between the electric motoreducer and the screw shaft. A variable preload mechanism allows various preload level to be set and measured dynamically by means of a load cell between the two nuts [74].

Funding

This research did not receive any specific grant from funding agencies in the public, commercial, or not-for-profit sectors.

Declaration of Interests

The authors declare no conflict of interest.

Colour preference

No colour images in the printed version.

Appendix A. Geometrical and lubricant's parameters

Table A.1: Ball screw parameters.

Geometrical parameter	Symbol	Value	Units
Screw pitch circle radius	r_m	8	mm
Screw lead	p	5	mm
Ball radius	r_b	1.5875	mm
Centre radius offset	H	0.0629	mm
Ogival offset	L	0.0505	mm
Screw and nut groove conformity factor	$f_{s,n}$	0.528	
Screw shaft moment of inertia around $\widehat{\mathbf{z}}$ axis	I_s	9.1893	$\mathrm{kg\,mm^2}$
Number of loaded turns	n_t	1.75	
Nut mass	M_n	0.275	kg
Total number of spheres per nut	Z_{tot}	30	
Number of effectively loaded spheres per nut	Z_{eff}	25	
Nominal helix angle	α_e	5.679	deg
Nominal contact angle	α	45.13	deg
Ball roughness [22]	σ_b	41.56	nm
Grooves roughness [22]	σ_g	11.56	nm
Screw, nut and ball elasticity modulus	$E_{s,n,b}$	210	GPa
Screw, nut and ball Poisson modulus	$\nu_{s,n,b}$	0.29	
Dynamic load	C_a	8.2	kN
Static load	C_0	13	kN
Critical screw angular speed	$\dot{\Omega}_{cr}$	18000	rpm

Table A.2: Properties of the lithium 12–hydroxystearate–thickened grease.

Property of Li/SS	Value
Base oil	Mineral oil (semi-synthetic)
Thickener agent	Lithium
NLGI grade	2
Mass fraction of thickener	0.17
Volume fraction of thickener	0.16
Grease viscosity at high shear rate [Pas]	0.1091
Grease density @ 25 °C [kg/m^3]	920
Base oil viscosity @ 25 °C [Pas]	0.07
Base oil viscosity @ 80 °C [Pas]	0.0045
Base oil density @ 25 °C [kg/m^3]	910
Bled oil viscosity @ 25 °C [Pas]	0.08
Bled oil viscosity @ 80 °C [Pas]	0.0051
Zero–shear–rate grease viscosity @ 25 °C [Pas]	8.9×10^5
Transition shear rate $\dot{\gamma}_c$ [s^{-1}]	1.4×10^{-4}
Grease yield stress @ 25 °C [Pa]	83
Storage modulus G' [Pa]	7.67×10^4
Base oil limiting shear stress τ_L [Pa]	2.5×10^6
Limiting shear stress pressure constant ξ	0.06
Yield shear stress temperature parameter b [°C]	50
Derived parameters	
Bled and base oil temperature–viscosity coefficient β [K^{-1}]	0.05
Base oil Roelands temperature–viscosity index S_0	1.1422
Bled oil Roelands temperature–viscosity index S_0	1.1208
Base oil Roelands pressure–viscosity index Z	0.6658
Bled oil Roelands pressure–viscosity index Z	0.6687
Base oil pressure–viscosity coefficient α_{pv} [Pa^{-1}]	23.805×10^{-9}
Bled oil pressure–viscosity coefficient α_{pv} [Pa^{-1}]	24.365×10^{-9}

References

[1] T. Ford, More-electric aircraft, Aircraft Engineering and Aerospace Technology 77 (2005).

[2] S. Hesse, G. Konrad, R. Reichel, I. Schäfer, P. Bourlier, M. Buff, An Electro - Mechanical Actuator for General Aviation Aircraft, in: Aerospace Technology Conference and Exposition, SAE, 2007, p. 11. doi:10.4271/2007-01-3900.

[3] J.-C. Maré, J. Fu, Review on signal-by-wire and power-by-wire actuation for more electric aircraft, Chinese Journal of Aeronautics 30 (2017) 857–870. doi:10.1016/j.cja.2017.03.013.

[4] A. R. Behbahani, K. J. Semega, Control Strategy for Electro-Mechanical Actuators Versus Hydraulic Actuation Systems for Aerospace Applications, in: Power System Conference, SAE, 2010, p. 13. doi:10.4271/2010-01-1747.

[5] M. Todeschi, Airbus - EMAs for flight actuation systems - perspectives, in: International Conference on Recent Advances in Aerospace Actuation Systems and Components, 2010, pp. 1–8.

[6] J.-C. Derrien, Electromechanical Actuator (EMA) Advanced Technologies for Flight Controls, in: 28Th

International Congress of the Aeronautical Sciences, 2012, pp. 1–10. doi:10.1007/s13398-014-0173-7.2. `arXiv:9809069v1`.

[7] J. Fu, J.-C. Maré, L. Yu, Y. Fu, Multi-level virtual prototyping of electromechanical actuation system for more electric aircraft, Chinese Journal of Aeronautics (2017). doi:10.1016/j.cja.2017.12.009.

[8] D. Howe, Magnetic actuators, Sensors and Actuators A: Physical 81 (2000) 268–274. doi:10.1016/S0924-4247(99)00174-0.

[9] S. Mauro, S. Pastorelli, T. Mohtar, Sensitivity Analysis of the Transmission Chain of a Horizontal Machining Tool Axis to Design and Control Parameters, Advances in Mechanical Engineering 6 (2014) 169064. doi:10.1155/2014/169064.

[10] S. Mauro, S. Pastorelli, E. Johnston, Influence of controller parameters on the life of ball screw feed drives, Advances in Mechanical Engineering 7 (2015) 1–11. doi:10.1177/1687814015599728.

[11] D. Ferrara, G. Jacazio, A. Mornacchi, M. Sorli, Robust mechatronic actuation system for UAV primary flight controls, in: ASME (Ed.), IMECE, ASME, Houston, Texas, USA, 2012, pp. 1–11.

[12] D. E. Blanding, A. J. Watanabe, Fault-tolerant electro-mechanical actuator having motor armatures to drive a ram and having an armature release mechanism, 2007.

[13] J. Bennett, B. Mecrow, D. Atkinson, G. Atkinson, Safety-critical design of electromechanical actuation systems in commercial aircraft, IET Electric Power Applications 5 (2011) 37. doi:10.1049/iet-epa.2009.0304.

[14] D. T. Nguyen, B. W. Behar, T. A. McKay, Jam-tolerant electromechanical actuator, 2014.

[15] M. Todeschi, L. Baxerres, Health monitoring for the flight control EMAs, in: IFAC-PapersOnLine, volume 48, Elsevier B.V., 2015, pp. 186–193. doi:10.1016/j.ifacol.2015.09.526.

[16] A. De Martin, G. Jacazio, G. Vachtsevanos, Anomaly Detection and Prognosis for Primary Flight Control EMAs, in: European Conference of the Prognostic and Health Management Society, 2016, pp. 1–9.

[17] G. Vachtsevanos, F. Lewis, M. Roemer, A. Hess, B. Wu, Intelligent Fault Diagnosis and Prognosis for Engineering Systems, John Wiley & Sons, Inc., Hoboken, NJ, USA, 2006. doi:10.1002/9780470117842.

[18] Y. M. Hussain, S. Burrow, L. Henson, P. Keogh, A Review of Techniques to Mitigate Jamming in Electromechanical Actuators for Safety Critical Applications, International Journal of Prognostics and Health Management (2018) 2153–2648.

[19] F. L. J. Linden, N. Dreyer, A. Dorkel, EMA Health Monitoring: An overview., Recent Advances in Aerospace Actuation Systems and Components (2016) 21–26.

[20] E. Balaban, A. Saxena, K. Goebel, Experimental data collection and modeling for nominal and fault conditions on electro-mechanical actuators, in: Annual Conference of the Prognostics and Health Management Society, 2009, pp. 1–15.

[21] E. Balaban, A. Saxena, P. Bansal, K. F. Goebel, P. Stoelting, S. Curran, A diagnostic approach for electro-mechanical actuators in aerospace systems, in: IEEEAC, 2009, p. 1345.

[22] C. C. Wei, W. L. Liou, R. S. Lai, Wear analysis of the offset type preloaded ball-screw operating at high speed, Wear 292-293 (2012) 111–123. doi:10.1016/j.wear.2012.05.024.

[23] T. Yoshida, Y. Tozaki, S. Matsumoto, Study on Load Distribution and Ball Motion of Ball Screw, 2003.

[24] C. E. Okwudire, Y. Altintas, Hybrid Modeling of Ball Screw Drives With Coupled Axial, Torsional, and Lateral Dynamics, Journal of Mechanical Design 131 (2009) 071002. doi:10.1115/1.3125887.

[25] C. E. Okwudire, Improved Screw–Nut Interface Model for High-Performance Ball Screw Drives, Journal of Mechanical Design 133 (2011) 041009. doi:10.1115/1.4004000.

[26] B. Lin, C. E. Okwudire, J. S. Wou, Low Order Static Load Distribution Model for Ball Screw Mechanisms including Effects of Lateral Deformation and Geometric Errors, Journal of Mechanical Design 140 (2018) 1–12. doi:10.1115/1.4038071.

[27] A. Oyanguren, P. Zahn, A. H. Alberdi, J. Larrañaga, A. Lechler, I. Ulacia, Preload variation due to temperature increase in double nut ball screws, Production Engineering 10 (2016) 529–537. doi:10.1007/s11740-016-0692-5.

[28] A. Oyanguren, J. Larrañaga, I. Ulacia, Thermo-mechanical modelling of ball screw preload force variation in different working conditions, International Journal of Advanced Manufacturing Technology

97 (2018) 723–739. doi:10.1007/s00170-018-2008-8.

[29] C. C. Wei, J. F. Lin, J.-H. Horng, Analysis of a ball screw with a preload and lubrication, Tribology International 42 (2009) 1816–1831. doi:10.1016/j.triboint.2008.12.013.

[30] C. C. Wei, R. S. Lai, Kinematical analyses and transmission efficiency of a preloaded ball screw operating at high rotational speeds, Mechanism and Machine Theory 46 (2011) 880–898. doi:10.1016/j.mechmachtheory.2011.02.009.

[31] J. Zhao, M. Lin, X. Song, H. Jiang, X. Wu, Investigation on the Precision Loss of Ball Screw Considering the Full Ball Load Distribution, IOP Conference Series: Materials Science and Engineering 422 (2018). doi:10.1088/1757-899X/422/1/012021.

[32] C. G. Zhou, Y. Ou, H. T. Feng, Z. T. Chen, Investigation of the precision loss for ball screw raceway based on the modified Archard theory, Industrial Lubrication and Tribology 69 (2017) 166–173. doi:10.1108/ILT-12-2015-0204.

[33] J. Liu, C. Ma, S. Wang, Precision loss modeling method of ball screw pair, Mechanical Systems and Signal Processing 135 (2020) 106397. doi:10.1016/j.ymssp.2019.106397.

[34] Q. Cheng, B. Qi, Z. Liu, C. Zhang, D. Xue, An accuracy degradation analysis of ball screw mechanism considering time-varying motion and loading working conditions, Mechanism and Machine Theory 134 (2019) 1–23. doi:10.1016/j.mechmachtheory.2018.12.024.

[35] C. C. Wei, J. F. Lin, Kinematic Analysis of the Ball Screw Mechanism Considering Variable Contact Angles and Elastic Deformations, Journal of Mechanical Design 125 (2003) 717–733. doi:10.1115/1.1623761.

[36] P. Li, X. Jia, J. Feng, H. Davari, G. Qiao, Y. Hwang, J. Lee, Prognosability study of ball screw degradation using systematic methodology, Mechanical Systems and Signal Processing 109 (2018) 45–57. doi:10.1016/j.ymssp.2018.02.046.

[37] G. H. Feng, Y. L. Pan, Establishing a cost-effective sensing system and signal processing method to diagnose preload levels of ball screws, Mechanical Systems and Signal Processing 28 (2012) 78–88. doi:10.1016/j.ymssp.2011.10.004.

[38] T. Nguyen, S. Ro, C. Song, J. Park, Study on preload monitoring of ball screw feed drive system using natural frequency detection, Journal of the Korean Society for Precision Engineering 35 (2018) 135–143. doi:10.7736/KSPE.2018.35.2.135.

[39] H. X. Zhou, C. G. Zhou, H. T. Feng, Y. Ou, Theoretical and experimental analysis of the preload degradation of double-nut ball screws, Precision Engineering 65 (2020) 72–90. doi:10.1016/j.precisioneng.2020.04.012.

[40] A. C. Bertolino, High Fidelity Model of Ball Screws to Support Model-based Health Monitoring, Ph.D. thesis, Ph.d. thesis, Politecnico di Torino, 2020.

[41] A. C. Bertolino, G. Jacazio, S. Mauro, M. Sorli, High Fidelity Model of a Ball Screw Drive for a Flight Control Servoactuator, in: ASME (Ed.), IMECE Volume 1: Advances in Aerospace Technology, volume 1, ASME, Tampa, Florida, USA, 2017, pp. 1–10. doi:10.1115/IMECE2017-70737.

[42] A. C. Bertolino, G. Jacazio, S. Mauro, M. Sorli, High fidelity model for efficiency calculation of ball screws for flight control actuators, in: Institut national des sciences appliquées Toulouse (Ed.), Recent Advances in Aerospace Actuation Systems and Components, Tolouse, France, 2018, pp. 153–163.

[43] A. C. Bertolino, M. Sorli, G. Jacazio, S. Mauro, Lumped parameters modelling of the EMAs' ball screw drive with special consideration to ball/grooves interactions to support model-based health monitoring, Mechanism and Machine Theory 137 (2019) 188–210. doi:10.1016/j.mechmachtheory.2019.03.022.

[44] A. C. Bertolino, S. Mauro, G. Jacazio, M. Sorli, Multibody dynamic model of a double nut preloaded ball screw mechanism with lubrication, in: ASME (Ed.), IMECE Volume 4: Dynamics, Vibration, and Control, ASME, Portland, OR, USA, 2020, pp. 1–11.

[45] ISO 3408-1:2006, Ball screws - Part 1: Vocabulary and designation, 2006.

[46] M. Budinger, A. Reysset, T. E. Halabi, C. Vasiliu, J.-C. Maré, Optimal preliminary design of electromechanical actuators, Proceedings of the Institution of Mechanical Engineers, Part G: Journal of Aerospace Engineering 228 (2014) 1598–1616. doi:10.1177/0954410013497171.

[47] A. Dellacasa, G. Jacazio, A. Zunino, EMADEF : a fully comprehensive analytical tool for the ini-

tial design of electro-mechanical servo-actuators for primary flight controls, in: Recent Advances in Aerospace Actuation Systems and Components, Tolouse, France, 2018, pp. 1–9.

[48] A. Verl, S. Frey, Correlation between feed velocity and preloading in ball screw drives, CIRP Annals - Manufacturing Technology 59 (2010) 429–432. doi:10.1016/j.cirp.2010.03.136.

[49] T. L. Nguyen, S. K. Ro, J. K. Park, Study of ball screw system preload monitoring during operation based on the motor current and screw-nut vibration, Mechanical Systems and Signal Processing 131 (2019) 18–32. doi:10.1016/j.ymssp.2019.05.036.

[50] C. G. Zhou, H. T. Feng, Z. T. Chen, Y. Ou, Correlation between preload and no-load drag torque of ball screws, International Journal of Machine Tools and Manufacture 102 (2016) 35–40. doi:10.1016/j.ijmachtools.2015.11.010.

[51] A. C. Bertolino, G. Jacazio, S. Mauro, M. Sorli, Developing of a Simscape Multibody Contact Library for Gothic Arc Ball Screws: A Three-Dimensional Model for Internal Sphere/Grooves Interactions, in: ASME (Ed.), IMECE Volume 4: Dynamics, Vibration, and Control, American Society of Mechanical Engineers, Salt Lake City, UT, USA, 2019, pp. 1–8. doi:10.1115/IMECE2019-10709.

[52] J.-F. Antoine, C. Visa, C. Sauvey, G. Abba, Approximate Analytical Model for Hertzian Elliptical Contact Problems, Journal of Tribology 128 (2006) 660. doi:10.1115/1.2197850.

[53] P. M. Lugt, Grease Lubrication in Rolling Bearings, John Wiley & Sons, Inc., 2013.

[54] G. Nijenbanning, C. H. Venner, H. Moes, Film thickness in elastohydrodynamically contacts, Wear 176 (1994) 217–229. doi:10.1016/0043-1648(94)90150-3.

[55] G. W. Stachowiak, A. W. Batchelor, Engineering tribology, 4th ed., Elsevier, 2014.

[56] P. K. Gupta, H. S. Cheng, D. Zhu, N. H. Forster, J. B. Schrand, Viscoelastic effects in MIL-L-7808-type lubricant, part I: Analytical formulation, Tribology Transactions 35 (1992) 269–274. doi:10.1080/10402009208982117.

[57] J. Castro, J. Seabra, Global and local analysis of gear scuffing tests using a mixed film lubrication model, Tribology International 41 (2008) 244–255. doi:10.1016/j.triboint.2007.07.005.

[58] D. Zhu, Y. Z. Hu, A computer program package for the prediction of ehl and mixed lubrication characteristics, friction, subsurface stresses and flash temperatures based on measured 3-d surface roughness, Tribology Transactions 44 (2001) 383–390. doi:10.1080/10402000108982471.

[59] T. E. Tallian, On competing failure modes in rolling contact, ASLE Transactions 10 (1967) 418–439. doi:10.1080/05698196708972201.

[60] D. N. Olaru, V. Puiu, Friction Torque and Efficiency in Ball-Screw Systems, Acta Tribologica 17 (2009) 25–29.

[61] D. Olaru, G. C. Puiu, L. C. Balan, V. Puiu, A New Model to Estimate Friction Torque in a Ball Screw System, in: Product Engineering, Kluwer Academic Publishers, Dordrecht, 2005, pp. 333–346. doi:10.1007/1-4020-2933-0_20.

[62] M. R. D. Balan, V. C. Stamate, L. Houpert, D. N. Olaru, The influence of the lubricant viscosity on the rolling friction torque, Tribology International 72 (2014) 1–12. doi:10.1016/j.triboint.2013.11.017.

[63] M. Bălan, L. Houpert, A. Tufescu, D. Olaru, Rolling Friction Torque in Ball-Race Contacts Operating in Mixed Lubrication Conditions, Lubricants 3 (2015) 222–243. doi:10.3390/lubricants3020222.

[64] W. Habchi, S. Bair, Is viscoelasticity of any relevance to quantitative EHL friction predictions?, Tribology International 135 (2019) 96–103. doi:10.1016/j.triboint.2019.02.048.

[65] Y. Zhou, R. Bosman, P. M. Lugt, A Model for Shear Degradation of Lithium Soap Grease at Ambient Temperature, Tribology Transactions 61 (2018) 61–70. doi:10.1080/10402004.2016.1272730.

[66] T. Cousseau, B. Graça, A. Campos, J. Seabra, Grease Aging Effects on Film Formation under Fully-Flooded and Starved Lubrication, Lubricants 3 (2015) 197–221. doi:10.3390/lubricants3020197.

[67] F. Cyriac, P. M. Lugt, R. Bosman, C. J. Padberg, C. H. Venner, Effect of Thickener Particle Geometry and Concentration on the Grease EHL Film Thickness at Medium Speeds, Tribology Letters 61 (2016) 1–13. doi:10.1007/s11249-015-0633-z.

[68] Hiwin Corp., Ball screws catalogue, 2020.

[69] NSK Corporation, Ball screw catalogue, 2020.

[70] KSS, Ball screws catalogue, 2020.

[71] ISO 3408-3:2006, Ball screws - Part 3: Acceptance conditions and acceptance tests, 2006.

[72] T. Harris, Rolling Bearing Analysis, 3rd ed., John Wiley & Sons, Inc., 1991.

[73] Y. F. Liu, J. Li, Z. M. Zhang, X. H. Hu, W. J. Zhang, Experimental comparison of five friction models on the same test-bed of the micro stick-slip motion system, Mechanical Sciences 6 (2015) 15–28. doi:10.5194/ms-6-15-2015.

[74] A. C. Bertolino, A. De Martin, G. Jacazio, S. Mauro, M. Sorli, Robust Design of a Test Bench for PHM Study of Ball Screw Drives, in: ASME (Ed.), IMECE Volume 1: Advances in Aerospace Technology, American Society of Mechanical Engineers, Salt Lake City, UT, USA, 2019, pp. 1–9. doi:10.1115/IMECE2019-10713.